Published in final edited form as:
Nat Phys. 2014 September ; 10(9): 683–690. doi:10.1038/nphys3040.

Forces driving epithelial wound healing

Agustí Brugués[#1], **Ester Anon**[#1,2], **Vito Conte**[#1], **Jim H. Veldhuis**[3], **Mukund Gupta**[6], **Julien Colombelli**[4], **José J. Muñoz**[5], **G. Wayne Brodland**[3], **Benoit Ladoux**[2,6,*], and **Xavier Trepat**[1,7,8,*]

[1]Institute for Bioengineering of Catalonia, Barcelona, Spain.

[2]Institut Jacques Monod (IJM), Université Paris Diderot, and Unité Mixte de Recherche 7592 CNRS, Paris, France

[3]Department of Civil and Environmental Engineering, University of Waterloo, Waterloo, Ontario, Canada.

[4]Institute for Research in Biomedicine (IRB Barcelona), Barcelona, Spain

[5]Laboratori de Càlcul Numèric, Department of Applied Mathematics III, Universitat Politècnica de Catalunya, Barcelona, Spain.

[6]Mechanobiology Institute (MBI), National University of Singapore, Singapore.

[7]Institució Catalana de Recerca i Estudis Avançats (ICREA), Barcelona, Spain.

[8]Unitat de Biofísica i Bioenginyeria, Facultat de Medicina, Universitat de Barcelona, and CIBERES, Spain

[#] These authors contributed equally to this work.

Abstract

A fundamental feature of multicellular organisms is their ability to self-repair wounds through the movement of epithelial cells into the damaged area. This collective cellular movement is commonly attributed to a combination of cell crawling and “purse-string” contraction of a supracellular actomyosin ring. Here we show by direct experimental measurement that these two mechanisms are insufficient to explain force patterns observed during wound closure. At early stages of the process, leading actin protrusions generate traction forces that point away from the wound, showing that wound closure is initially driven by cell crawling. At later stages, we observed unanticipated patterns of traction forces pointing towards the wound. Such patterns have strong force components that are both radial and tangential to the wound. We show that these force

[*]Corresponding authors: Prof. Xavier Trepat, Institute for Bioengineering of Catalonia C/ Baldiri Reixac 15-21 Barcelona 08028 Spain Tel: +34934020265 xtrepat@ibecbarcelona.eu; Prof. Benoit Ladoux Institut Jacques Monod, Université Paris Diderot & CNRS UMR 7592 Batiment Buffon 15 rue Hélène Brion 75013 Paris, France benoit.ladoux@univ-paris-diderot.fr.

AUTHOR CONTRIBUTIONS

A.B., E.A., J.C., B.L and X.T. designed experiments; A.B. and E.A. performed experiments; A.B. analyzed experimental data; A.B., V.C. and J.J.M. developed computational tools for data and stress analysis; M.G. analyzed micropillar data; J.C. contributed technology; V.C., J.H.V. and G.W.B built computational models and performed simulations; A.B., E.A., V.C., J.J.M, G.W.B., B.L. and X.T wrote the manuscript; all authors discussed and interpreted results and commented on the manuscript; B.L. and X.T. conceived and supervised the project.

Europe PMC Funders Author Manuscripts

components arise from tensions transmitted by a heterogeneous actomyosin ring to the underlying substrate through focal adhesions. The structural and mechanical organization reported here provides cells with a mechanism to close the wound by cooperatively compressing the underlying substrate.

Wound healing is a central physiological process that involves a complex interplay between inflammation and tissue remodeling[1-3]. Impaired wound healing has a significant clinical impact in a variety of widespread diseases such as diabetes, chronic inflammatory disorders, vascular diseases, and auto-immune diseases[2-4]. Moreover, there is a well-established association between aberrant wound healing and cancer progression[5].

A crucial step of the wound healing response is the restoration of a continuous epithelial layer to recover tissue homeostasis, regain barrier integrity, and protect organisms from infection[4,6]. Epithelial repair is achieved through the collective movement of wound-bordering cells into the wound bed. To account for this collective movement, two main mechanisms are commonly invoked[1-3,6-11]. The first one is the assembly of a supracellular actomyosin ring at the wound margin, whose contraction drives the wound edges together like a purse-string[10,12-16]. The second mechanism is collective migration of marginal and submarginal cells led by lamellipodial and filopodial protrusions[17-21].

Extensive evidence supports the coexistence of a supracellular actomyosin ring and lamellipodial protrusions at the wound margin[8-11,22,23]. How these cytoskeletal structures drive wound closure remains incompletely understood, however, because underlying physical forces have not been accessible to direct experimental observation. To provide the first maps of these physical forces, here we combined traction force microscopy and laser ablation. We seeded a monolayer of MDCK cells stably expressing LifeAct-GFP on top of a soft collagen-coated polyacrylamide gel containing fluorescent bead markers. Once the monolayer reached confluence and relatively high density, a cluster of ~20 cells (~5000 μm^2) was ablated by recurrently targeting apical cell surfaces with a sub-nanosecond pulsed laser (Fig. 1a-c, Methods). Immediately after ablation, targeted cells lost a substantial amount of their F-actin content and surrounding cells retracted outwardly.

Following rapid tissue retraction, cells began to invade the wound area and to extrude ablated cells (Supplementary video 1). The onset of this wound closure phase involved rapid protrusion of lamellipodia and filopodia toward the wound area (Fig. 1d). With a delay of ~15 minutes, cell protrusion was followed by accumulation of actin and myosin at the wound edge (Fig. 1e, g-l). Formation of this supracellular actomyosin ring did not inhibit cell protrusions, which remained visible throughout closure (Fig. 1d-f). Both marginal and submarginal cells progressively acquired an elongated shape and constricted their front edge so as to create a rosette-like geometry by the end of wound closure (Fig. 1f). Throughout the process, cells remained tightly connected to their neighbors through adherens junctions and tight junctions (Supplementary Fig. 1a,b).

To map cell velocities during wound healing we used particle imaging velocimetry on consecutive image pairs. Resulting maps revealed that throughout the closure process cell velocities pointed uniformly towards the wound and were highest at the leading edge (Fig.

Europe PMC Funders Author Manuscripts

1m-p). To analyze systematically the spatiotemporal evolution of cell velocity maps we computed the average radial velocity as a function of distance from the wound edge and represented this average as spatiotemporal kymographs (Fig. 1q, Supplementary methods). Kymographs confirmed systematic gradients of radial velocity decaying away from the leading edge. However, the velocity of each cell row around the wound exhibited a non-monotonic time evolution (Fig. 1r) with a maximum at ~30 minutes after the onset of wound healing (~10 min after starting image acquisition). In contrast with the case of expanding monolayers[24], we did not observe a significant delay in the onset of cell motion between adjacent cell rows, suggesting a mechanism for rapid intercellular coordination specific to wound closure.

To elucidate the mechanisms driving cellular motions we turned to the measurement of cell-substrate traction forces using monolayer traction microscopy[21] (Fig. 2, Supplementary video 2). The orientation of these forces depended on the curvature of the wound edge. To illustrate this observation we color-coded traction maps based on the sign of their radial component (Fig. 2a-c). Regions of the leading edge exhibiting a convex contour displayed pronounced protrusive activity and traction forces pointing away from the wound (Fig. 2a). By contrast, regions exhibiting a concave contour showed little protrusive activity, an accumulation of actin at the leading edge, and traction forces pointing toward the wound (Fig. 2a). As wound closure progressed, the contour of the leading edge became progressively smoother, and tractions pointing towards the wound became ubiquitous (Fig. 2b,c). The radial component of traction forces increased in magnitude with wound curvature and, as closure progressed, this dependence became stronger (Supplementary Fig. 2).

To confirm the results obtained with traction force microscopy on continuous substrates, we carried out wound closure experiments in cell monolayers seeded on top of an array of flexible micropillars[19,25-27]. Because each micropillar is mechanically uncoupled from its neighbors, traction forces can be computed from a direct measurement of micropillar deflection. Force maps obtained from micropillar deflections confirmed the coexistence of inward- and outward-pointing traction forces at the leading edge of the monolayer (Fig. 2h, Supplementary video 3). Given the agreement between traction force microscopy on continuous substrates and on micropillar arrays, we used the former technique in the remainder of the study.

To isolate systematic force patterns from force fluctuations we computed the average radial ($T_{\perp}$) and tangential ($T_{\parallel}$) traction force components as a function of distance from the wound edge. Resulting kymographs displayed a remarkable spatiotemporal force pattern (Fig. 2d,e). At the front of the first cell row, the radial force kymograph exhibited a boundary layer of tractions pointing away from the wound up to the end of the closure process. Immediately behind this boundary layer of outward-pointing tractions, but still within the front of the first cell row, there emerged a second layer with a net inward-pointing component increasing in magnitude with time (Fig. 2d). Tractions within this layer were not purely radial, however, and their tangential component was on average larger than the radial one (Fig. 2e). Further away from the leading edge, traction forces were weak but systematically pointing away from the wound, thus showing that crawling forces are not restricted to the first cell row.

A boundary layer of net outward-pointing tractions, which we refer hereafter as outward-pointing traction layer (OPTL), has been previously observed in expanding cellular monolayers[19,21]. It has also been reported in monolayers migrating along concave and convex islands on which cells could not adhere[28] and at the leading edge of invading supracellular fingers[27,29,30]. This type of force pattern is typically associated with lamellipodial protrusions[19,21,27,29,30]. By contrast, the observation of a boundary layer of inward pointing traction forces, which we refer hereafter as inward-pointing traction layer (IPTL), is altogether new. The OPTL and the IPTL do not originate solely from averaging two distinct cell populations, one comprising cells favoring protrusions and one comprising cells favoring the actomyosin ring. Instead, outward- and inward-pointing tractions were seen to coexist at different distances from the leading edge of individual cells (Fig. 2a-c, g). The coexistence of these two distinct force patterns of opposite sign creates a contractile dipole at the tip of protruding leading cells. This dipole was confirmed by monitoring the time evolution of radial forces in micropillar arrays, which showed a clear succession of two phases; in the first phase, cells pulled the pillars towards the monolayer, consistent with the OPTL, whereas in the second phase they pushed them toward the wound, consistent with the IPTL (Fig 2i). Contractile dipoles between the leading and trailing edges have been extensively reported in single cells migrating in isolation[31-33]. By contrast, the contractile dipoles reported here are restricted to the leading edge of the first cell row. This type of dipole is absent in single cells migrating in isolation[31-33], in cells migrating collectively during monolayer expansion[19,21,26], in invasive supracellular fingers [27,29,30], and in cells enveloping non-adherent islands[28].

The stiffness of the cellular microenvironment has been extensively shown to regulate cell migration and traction forces[34-36]. We next inquired whether patterns of traction forces and wound healing kinematics were sensitive to the stiffness of the underlying gel. To address this question, we studied wound healing in cell monolayers seeded on 3 kPa substrates (3-fold softer than controls). On these soft substrates, cells also assembled a supracellular actomyosin cable, extended multiple protrusions in the wound area, and generated an OPTL at the leading edge and an IPTL immediately behind it (Supplementary Fig. S3a-d). Cells on soft substrates also showed similar sealing times than those on stiff substrates (Supplementary Fig. S3e). This lack of sensitivity of wound healing forces and kinematics with substrate stiffness is in sharp contrast with the case of single cells migrating in isolation, which showed significantly slower migration velocities on soft substrates (Supplementary Fig. S3f).

A candidate mechanism to explain the IPTL is the transmission of contractile force from the actomyosin ring to the substrate. To study this possibility we first focused on the colocalization of the actomyosin ring and the IPTL. Confocal z-stacks revealed that the actomyosin ring was located basally (Fig. 1g-l, Fig. 2g) and its assembly coincided in time and space with the emergence of the IPTL. Such colocalization between the ring and the IPTL persisted throughout the closure process (Fig. 2d-f). This evidence strongly suggests that the IPTL originates from the transmission of contractile forces from the basal ring to the underlying substrate.

To further ascertain the origin of the IPTL, we studied the dynamics of wound closure in the absence of a supracellular actomyosin ring. To prevent ring formation, we treated cells with medium containing 4 mM of calcium chelator EGTA for 1 hour before laser ablation and reduced the concentration to 2 mM during the experiment (Fig. 3, Supplementary video 4). Calcium chelation weakened cell-cell junctions behind the leading edge but did not fully disrupt them as shown by the presence of E-cadherin and ZO-1 at intercellular contacts (Supplementary Fig. 1c,d). By contrast, calcium chelation prevented the assembly of a supracellular actomyosin ring at the wound edge (Fig. 3a-c). Under these conditions, the sealing time was similar to control wounds (Fig. 3l) but submarginal cells moved faster (Fig. 3a-e) and exhibited a loss of directionality (Fig. 3f). Importantly, impairment of the actomyosin ring prevented the emergence of the IPTL (Fig. 3j). Instead, average tractions pointed away from the wound, giving rise to an OPTL that spanned multiple cell rows, which indicates a cell-crawling mechanism involving cooperative force transmission in the radial direction as in a tug-of-war[21] (Fig. 3g-k).

Besides preventing formation of the actomyosin ring, calcium chelation mediates other effects that might also contribute to the loss of the IPTL. Thus, to further ascertain that the IPTL is caused by transmission of forces from the ring to the substrate, we ablated the ring at multiple locations and studied resulting changes in traction forces (Fig. 4a, Supplementary video 5). Immediately after ablation, we observed a sudden reduction of inward-pointing traction forces under the ring and behind it (Fig. 4b,c). This reduction became more pronounced with time and, 30s after ablation, inward-pointing traction forces were abrogated (Fig. 4f). Taken together, our results establish that the IPTL originates from transmission of forces from the ring to the substrate.

Our findings put forward a physical picture in which the OPTL originates from lamellipodial forces, while the IPTL originates from transmission of forces from the ring to the substrate. To evaluate whether these force contributions are sufficient to recapitulate the observed wound closure dynamics we developed a 2-D cellular *in silico* model (Supplementary note 1). To build the model, lamellipodia and gel tractions were added to a finite element-based γ-μ model of cell mechanics[37,38] (Supplementary Figs. S7, S8). Tensions arising from general cortical contraction and actomyosin ring forces were assumed to act along the cell boundaries while the cytoplasm in the cells was assumed to be viscous and incompressible. Lamellipodia were assumed to arise randomly from any cell edge, but particularly from the edges along the wound perimeter, and to attach to the underlying gel. Viscous drag was assumed to act between the cells and the gel.

Under such assumptions, the model shows that the wound can close either through cell crawling or through purse-string contraction (Supplementary Fig. 9a-d). Lamellipodial protrusions generate an OPTL while transmission of tension from the ring to the substrate generates an IPTL. If both mechanisms coexist, the model is able to recapitulate wound closure kinematics as well as patterns of traction forces in the radial direction (Supplementary Fig. 9e,f). However, the model is unable to explain the striking observation of large traction forces in the tangential direction (Fig. 2b,e). In fact, if the ring had a circular contour and carried constant tension it would produce no tangential traction forces

at all. This suggests an additional mechanism needs to be accounted for to fully explain traction force generation at the ring.

To address this issue we focused on the structure and localization of focal adhesions. At the leading tip of lamellipodia, staining of paxillin revealed that focal adhesions were perpendicular to the cell edge (Fig. 5a-d). This geometrical organization is characteristic of lamellipodia-driven cell migration[24,29,30] and is consistent with the force pattern observed at the OPTL. We also observed an accumulation of focal adhesions underneath the actomyosin ring, which is consistent with our conclusion that transmission of force from the ring to the substrate gives rise to the IPTL. Importantly, a large fraction of focal adhesions under the ring were tangential to the wound (Fig. 5e-h,l, Supplementary Fig. 4). We confirmed this observation in wound closure experiments using LifeAct-Ruby cells expressing talin-GFP (Fig. 5i-k, Supplementary video 6). These measurements suggest that the source of high tangential tractions in force kymographs is the transmission of tension from the ring to the substrate at tangential focal adhesions (Fig 2e). This was confirmed by ablation of the ring, which caused an instantaneous drop in tangential traction forces (Fig. 4d,e,g).

If the ring is transmitting forces to the substrate in the tangential direction, then the tension it carries must be heterogeneous in space. To assess tension heterogeneity in the ring, we computed the 2D stress tensor (σ) at the gel interface with the epithelium. This tensor measures the extent to which traction forces generated by cells produce tension or compression at any given point and direction of the gel surface (Supplementary Methods). To take into account the geometry of the experiments, we focused on the normal components of σ in the directions that are perpendicular (σ_{rr}) and tangential (σ_{tt}) to the actomyosin ring. The resulting stress maps, which are not to be confused with traction maps, showed strong spatial heterogeneities under the actomyosin ring with a sharp alternation between compressive and tensile stresses (Fig. 5m,n,p,q). These spatial heterogeneities are inconsistent with current understanding of wound closure mechanisms based on a continuous ring carrying homogenous tension. Rather, they point to a ring structure that is heterogeneous in space and transmits part of its contractile tension to the substrate through force dipoles oriented tangentially to the wound edge. When this key feature was added to our computational model, kymographs of all force components were successfully reproduced (Supplementary note 1, Supplementary Fig. 9g-h).

Exerting traction forces tangentially to the wound would seem counterproductive to drive the cell sheet forward and to extrude damaged cells upwards. Analysis of substrate displacements within the underlying gel leads to a quite different conclusion, however. When a contractile force dipole is applied to the surface of an elastic material with positive Poisson's ratio, it generates material displacements toward the dipole centre and normally to the dipole's direction. If several such dipoles are arranged in an annular geometry, their contraction will result in a net displacement of the gel surface toward the center of the ring (Fig. 5o,r, Supplementary note 2, Supplementary Fig. 11a). Thus by applying traction forces tangentially to the wound, cells create net substrate displacements that are radial and point toward the wound, thereby contributing to drag the cell sheet into the wound area (Supplementary note 2). These displacement patterns are mechanically analogous to those

that would result from the active contraction of the tissue underlying the wound, as previously proposed in experimental models of embryonic wound healing[7].

Heterogeneous and anisotropic substrate deformations have been extensively shown to guide cell migration through mechanotransduction processes that remain poorly understood[39-42]. In the case of MDCK cell sheets, for example, self-generated substrate displacements have been shown to precede in time cellular velocities[40]. Thus, in addition to dragging the cell sheet forward passively, the inward-pointing substrate displacements reported here are also likely to steer cell migration through active mechanotransduction mechanisms. We note that these mechanisms are enhanced on soft substrates, where displacements are higher. As such, they appear as reasonable candidates to explain why isolated cells are slower on soft substrates whereas wound closure rates are paradoxically not (Fig S3e,f).

Our experimental and computational findings establish a new quantitative scenario for the mechanisms driving wound closure in an epithelial sheet. According to this scenario, collective cell crawling is responsible for the initial steps of wound closure but the latest stages of the process involve the cooperation between cell crawling and contraction of a supracellular actomyosin ring at the leading edge. Our study reveals that this supracellular ring is a much more versatile structure than previously thought and serves at least two purposes. First it contributes to wound closure through its well-known purse-string mechanism[2,3,8-10,15]. Second, it transmits part of its contractile force to the substrate through focal adhesions that are mainly tangential to the wound. These contractile forces induce a displacement of the underlying gel toward the wound area and thus tend to steer the monolayer forward. The leading edge dynamics and force patterns reported here are qualitatively distinct from any previous observation in single or collective cell systems[19,21,26-29,32,33,43,44]. As such, they constitute a starting point in the search for new mechanotransduction strategies in wound closure as well as in the broader context of morphogenesis.

METHODS

Traction microscopy

Unless noted otherwise, tractions were measured by Fourier-transform traction microscopy with finite gel thickness as described in Trepat et al.[21]. An interrogation window of 32×32 pixels and an overlap of 0.75 were used for the analysis of bead displacements.

PA gel preparation

Polyacrylamide (PA) gels were prepared by activating glass bottom Petri dishes by incubation with Bind Silane dissolved in acetic acid and ethanol (following the proportion 1:1:14) during 10 min. After rinsing with ethanol, dishes were allowed to air dry. Meanwhile, a mixture of 240 μl NHS (10 mg/ml), 2.5 μl APS (10%), 0.25 μl TEMED, 12 μl 0.2 μm red beads (Fluospheres, Invitrogen), 126.4 μl of HEPES 10 mM, 93.75 μl of acrylamide (40%), and 25 μl of bisacrylamide (2%) was prepared, to obtain gels of 9 KPa in Young's modulus[45]. 12 μl of this mixture were added to a Petri dish, flattened with an 18 mm glass coverslip and allowed to polymerize for 30 to 45 min. Deionized water was then

added to peel off the glass coverslip. Collagen I was added at 0.1 mg/ml and incubated at 4°C overnight.

Micropillar arrays

In selected experiments, traction forces were measured using a dense array of fibronectin-coated PDMS micropillars[19,25,27]. Micropillars (3 μm height, 1 μm diameter, 2 μm center to center distance) arranged in a hexagonal grid were molded from a silicon master as previously described[19,25,27]. Custom-made multiple-particle tracking software was used to calculate the deflection of the pillars from the undeformed array.

Focal adhesion analysis

Paxillin fluorescent images obtained by immunostaining were segmented by thresholding. Segmented regions were fitted to an ellipse to obtain the eccentricity and orientation. Only adhesions with sizes between 5 and 100 pixels and eccentricity above 0.5 were included in the analysis.

Cell culture

Madin Darby canine kidney (MDCK) II cells and stable cell lines expressing LifeAct-GFP or LifeAct-Ruby were cultured with Dulbecco's modified Eagle's medium supplemented with 10% fetal bovine serum, 100 U/ml of penicillin, 100 μg/ml of streptomycin. Selection antibiotic geneticin was added at 0.5 mg/ml for LifeAct stable cell lines. Cells were maintained at 37°C in a humidified atmosphere with 5% of CO_2.

Laser ablation and time-lapse imaging

The set-up used is described in Colombelli et al[46]. After wounding, time-lapse imaging of the gel surface and of the overlying cells was performed using an inverted Nikon confocal microscope, equipped with an incubator to maintain the samples at 37°C and 5% CO_2. Laser cutting and traction microscopy were performed in different setups. As such there was an average delay of ~20 min between wounding and the beginning of image acquisition. Image size was 512×512 pixels.

Velocity measurements

Velocity maps were obtained by PIV with continuous window shift with an interrogation window of 64×64 pixels and overlap of 0.75.

Transfection

To image talin during wound closure we used CellLight® talin-GFP. Cells were seeded at low density. When cells were completely attached to the substrate we added 10 μl of the product in 2 ml of medium. Cells were used 16h after transfection.

Immunofluorescence

Cells were fixed with 4% paraformaldehyde (in PBS) for 15 min at room temperature (in EGTA experiments paraformaldehyde was diluted in a 4mM EGTA solution). Permeabilization was achieved by incubating with 0.25% Triton X100 (in PBS) for 20 min

Europe PMC Funders Author Manuscripts

Europe PMC Funders Author Manuscripts

at room temperature. Cells were saturated with 1% BSA (in PBS) and incubated during 30 min. In the case of Paxillin, 10% FBS (in PBS) was used as blocking solution and cells were incubated during 60 min. Primary antibodies were added with corresponding blocking solution at 1:1000 dilution for ZO-1 and E-cadherin and 1:200 for paxillin and phospho-MLC and incubated for 1-2 hours. Secondary antibodies were added at 1:200 dilution (with 1:1000 of Phalloidin if needed) and incubated for 1-2 hours.

Supplementary Material

Refer to Web version on PubMed Central for supplementary material.

ACKNOWLEDGEMENTS

We thank M. Bintanel for technical assistance and P. Roca-Cusachs and members of the Trepat Lab for discussions. This research was supported by the Spanish Ministry for Economy and Competitiveness (BFU2012-38146 to XT, Juan de la Cierva Fellowship JCI-2012-15123 to VT), the European Research Council (Grant Agreement 242993, XT), the Agence Nationale de la Recherche (ANR 2010 BLAN 1515, BL), the Human Frontier Science Program (grant RGP0040/2012, BL), the Mechanobiology Institute of Singapore (BL), and the Natural Sciences and Engineering Research Council of Canada (NSERC, JHV and GWB).

REFERENCES

1. Shaw TJ, Martin P. Wound repair at a glance. J Cell Sci. 2009; 122:3209–3213. [PubMed: 19726630]
2. Sonnemann KJ, Bement WM. Wound Repair: Toward Understanding and Integration of Single-Cell and Multicellular Wound Responses. Annu Rev Cell Dev Biol. 2011; 27:237–263. [PubMed: 21721944]
3. Cordeiro, J. o. V.; Jacinto, A. n. The role of transcription-independent damage signals in the initiation of epithelial wound healing. Nat Rev Mol Cell Biol. 2013; 14:249–262.
4. Crosby LM, Waters CM. Epithelial repair mechanisms in the lung. Am J Physiol Lung Cell Mol Physio. 2010; 298:L715–L731.
5. Arwert EN, Hoste E, Watt FM. Epithelial stem cells, wound healing and cancer. Nat Rev Cancer. 2012; 12:170–180. [PubMed: 22362215]
6. Kuipers D, et al. Epithelial repair is a two-stage process driven first by dying cells and then by their neighbours. J Cell Sci. 2014; 127:1229–1241. [PubMed: 24463819]
7. Davidson LA, Ezin AM, Keller R. Embryonic wound healing by apical contraction and ingression in Xenopus laevis. Cell Motil Cytoskeleton. 2002; 53:163–176. [PubMed: 12211099]
8. Anon E, et al. Cell crawling mediates collective cell migration to close undamaged epithelial gaps. Proc. Natl. Acad. Sci. U.S.A. 2012; 109:10891–10896. [PubMed: 22711834]
9. Klarlund JK. Dual modes of motility at the leading edge of migrating epithelial cell sheets. Proc. Natl. Acad. Sci. U.S.A. 2012; 109:15799–15804. [PubMed: 23019364]
10. Tamada M, Perez TD, Nelson WJ, Sheetz MP. Two distinct modes of myosin assembly and dynamics during epithelial wound closure. J Cell Biol. 2007; 176:27–33. [PubMed: 17200415]
11. Abreu-Blanco MT, Verboon JM, Liu R, Watts JJ, Parkhurst SM. Drosophila embryos close epithelial wounds using a combination of cellular protrusions and an actomyosin purse string. J Cell Sci. 2012
12. Martin P, Lewis J. Actin cables and epidermal movement in embryonic wound healing. Nature. 1992; 360:179–183. [PubMed: 1436096]
13. Bement WM, Forscher P, Mooseker MS. A novel cytoskeletal structure involved in purse string wound closure and cell polarity maintenance. J Cell Biol. 1993; 121:565–578. [PubMed: 8486737]
14. Jacinto A, Woolner S, Martin P. Dynamic Analysis of Dorsal Closure in Drosophila: From Genetics to Cell Biology. Dev Cell. 2002; 3:9–19. [PubMed: 12110163]

15. Hutson MS, et al. Forces for Morphogenesis Investigated with Laser Microsurgery and Quantitative Modeling. Science. 2003; 300:145–149. [PubMed: 12574496]
16. Antunes M, Pereira T, Cordeiro JV, Almeida L, Jacinto A. Coordinated waves of actomyosin flow and apical cell constriction immediately after wounding. J Cell Biol. 2013; 202:365–379. [PubMed: 23878279]
17. Fenteany G, Janmey PA, Stossel TP. Signaling pathways and cell mechanics involved in wound closure by epithelial cell sheets. Curr Biol. 2000; 10:831–838. [PubMed: 10899000]
18. Omelchenko T, Vasiliev JM, Gelfand IM, Feder HH, Bonder EM. Rho-dependent formation of epithelial “leader” cells during wound healing. Proc. Natl. Acad. Sci. U.S.A. 2003; 100:10788–10793. [PubMed: 12960404]
19. Roure, O. d., et al. Force mapping in epithelial cell migration. Proc. Natl. Acad. Sci. U.S.A. 2005; 102:2390–2395. [PubMed: 15695588]
20. Poujade M, et al. Collective migration of an epithelial monolayer in response to a model wound. Proc. Natl. Acad. Sci. U.S.A. 2007; 104:15988–15993. [PubMed: 17905871]
21. Trepat X, et al. Physical forces during collective cell migration. Nat Phys. 2009; 5:426–430.
22. Meghana C, et al. Integrin adhesion drives the emergent polarization of active cytoskeletal stresses to pattern cell delamination. Proc. Natl. Acad. Sci. U.S.A. 2011; 108:9107–9112. [PubMed: 21571643]
23. Cochet-Escartin O, Ranft J, Silberzan P, Marcq P. Border Forces and Friction Control Epithelial Closure Dynamics. Biophys J. 2014; 106:65–73. [PubMed: 24411238]
24. Serra-Picamal X, et al. Mechanical waves during tissue expansion. Nat Phys. 2012; 8:628–634.
25. Tan JL, et al. Cells lying on a bed of microneedles: An approach to isolate mechanical force. Proc. Natl. Acad. Sci. U.S.A. 2003; 100:1484–1489. [PubMed: 12552122]
26. Saez A, et al. Traction forces exerted by epithelial cell sheets. J. Phys.: Condens. Matter. 2010; 22
27. Reffay M, et al. Interplay of RhoA and mechanical forces in collective cell migration driven by leader cells. Nat Cell Biol. 2014; 16:217–223. [PubMed: 24561621]
28. Kim JH, et al. Propulsion and navigation within the advancing monolayer sheet. Nat Mater. 2013; 12:856–863. [PubMed: 23793160]
29. Vedula SRK, et al. Emerging modes of collective cell migration induced by geometrical constraints. Proc. Natl. Acad. Sci. U.S.A. 2012
30. Vedula SRK, et al. Epithelial bridges maintain tissue integrity during collective cell migration. Nat Mater. 2013; 13:87–96. [PubMed: 24292420]
31. Dembo M, Wang YL. Stresses at the cell-to-substrate interface during locomotion of fibroblasts. Biophys J. 1999; 76:2307–2316. [PubMed: 10096925]
32. Wang N, et al. Cell prestress. I. Stiffness and prestress are closely associated in adherent contractile cells. Am J Physiol Cell Physiol. 2002; 282:C606–C616. [PubMed: 11832346]
33. Bastounis E, et al. Both contractile axial and lateral traction force dynamics drive amoeboid cell motility. J Cell Biol. 2014; 204:1045–1061. [PubMed: 24637328]
34. Lo CM, Wang HB, Dembo M, Wang YL. Cell movement is guided by the rigidity of the substrate. Biophys J. 2000; 79:144–152. [PubMed: 10866943]
35. Saez A, Ghibaudo M, Buguin A, Silberzan P, Ladoux B. Rigidity-driven growth and migration of epithelial cells on microstructured anisotropic substrates. Proc. Natl. Acad. Sci. U.S.A. 2007; 104:8281–8286. [PubMed: 17488828]
36. Ng MR, Besser A, Danuser G, Brugge JS. Substrate stiffness regulates cadherin-dependent collective migration through myosin-II contractility. J Cell Biol. 2012; 199:545–563. [PubMed: 23091067]
37. Chen HH, B. GW. Cell-level finite element studies of viscous cells in planar aggregates. J Biomech Eng. 2000; 122:394–401. [PubMed: 11036563]
38. Brodland GW, Viens D, Veldhuis JH. A new cell-based FE model for the mechanics of embryonic epithelia. Comput Methods Biomech Biomed Engin. 2007; 10:121–128. [PubMed: 18651278]
39. Reinhart-King CA, Dembo M, Hammer DA. Cell-Cell Mechanical Communication through Compliant Substrates. Biophys J. 2008; 95:6044–6051. [PubMed: 18775964]

40. Angelini TE, Hannezo E, Trepat X, Fredberg JJ, Weitz DA. Cell Migration Driven by Cooperative Substrate Deformation Patterns. Phys. Rev. Lett. 2010; 104

41. Plotnikov SV, Pasapera AM, Sabass B, Waterman CM. Force Fluctuations within Focal Adhesions Mediate ECM-Rigidity Sensing to Guide Directed Cell Migration. Cell. 2012; 151:1513–1527. [PubMed: 23260139]

42. Roca-Cusachs P, Sunyer R, Trepat X. Mechanical guidance of cell migration: lessons from chemotaxis. Curr Opin Cell Biol. 2013; 25:543–549. [PubMed: 23726023]

43. Behrndt M, et al. Forces Driving Epithelial Spreading in Zebrafish Gastrulation. Science. 2012; 338:257–260. [PubMed: 23066079]

44. Fernandez-Gonzalez R, Zallen JA. Wounded cells drive rapid epidermal repair in the early Drosophila embryo. Mol. Biol. Cell. 2013; 24:3227–3237. [PubMed: 23985320]

45. Yeung T, et al. Effects of substrate stiffness on cell morphology, cytoskeletal structure, and adhesion. Cell Motil Cytoskeleton. 2005; 60:24–34. [PubMed: 15573414]

46. Colombelli J, Grill SW, Stelzer EHK. Ultraviolet diffraction limited nanosurgery of live biological tissues. Rev Sci Instrum. 2004; 75:472–478.

Europe PMC Funders Author Manuscripts

Europe PMC Funders Author Manuscripts

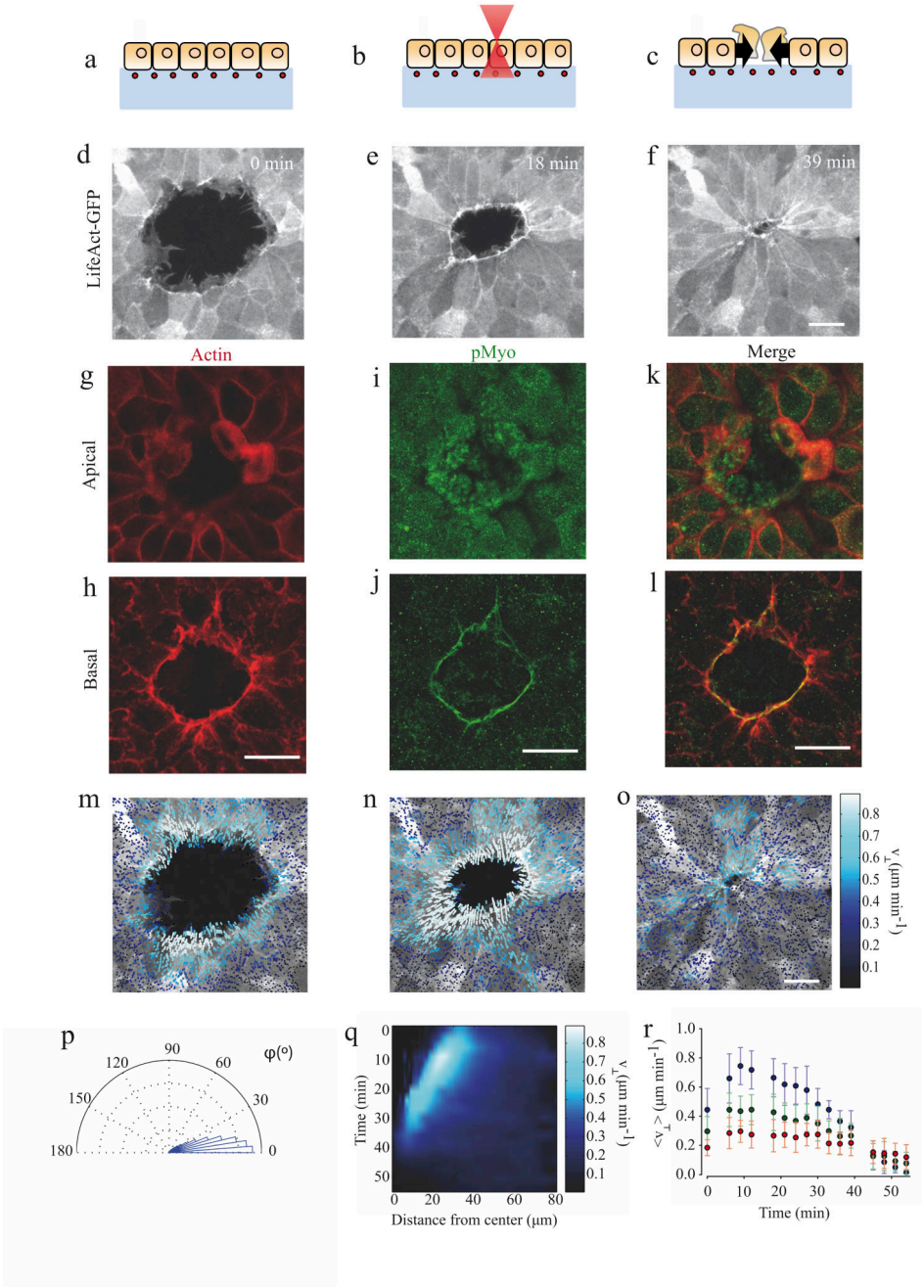

Figure 1. Cell morphology and kinematics during wound healing

(a-c) Scheme of the experimental design. (d-f) Time course of wound closure in LifeAct-GFP MDCK cells. Images are maximum projections of confocal z-stacks. Staining of phalloidin and pMyo at the apical (g-k) and basal (h-l) planes. (m-o) Vectorial representation of cell velocities measured by PIV at the same time points as in d-f. (p) Distribution of the angle φ between cell velocities and the direction normal to the wound edge. Data are a pool of all time points for one experiment. (q) Kymograph of the radial component of cell velocities (see supplementary methods). (r) Time evolution of cell velocities as a function of

the distance from the leading edge. The Time axis indicates the time after the beginning of image acquisition (~20 min after wounding). Each dataset represents the average radial velocity within concentric rings of width 15 μm (blue for cells located between 0-15 μm from the leading edge, green for 15-30 μm, red for 30-45 μm). Error bars represent standard deviation. Missing time points in (r) are due to image refocusing. Data for these time points have been interpolated in (q) to help visualization. All scale bars are 20μm.

Europe PMC Funders Author Manuscripts

Europe PMC Funders Author Manuscripts

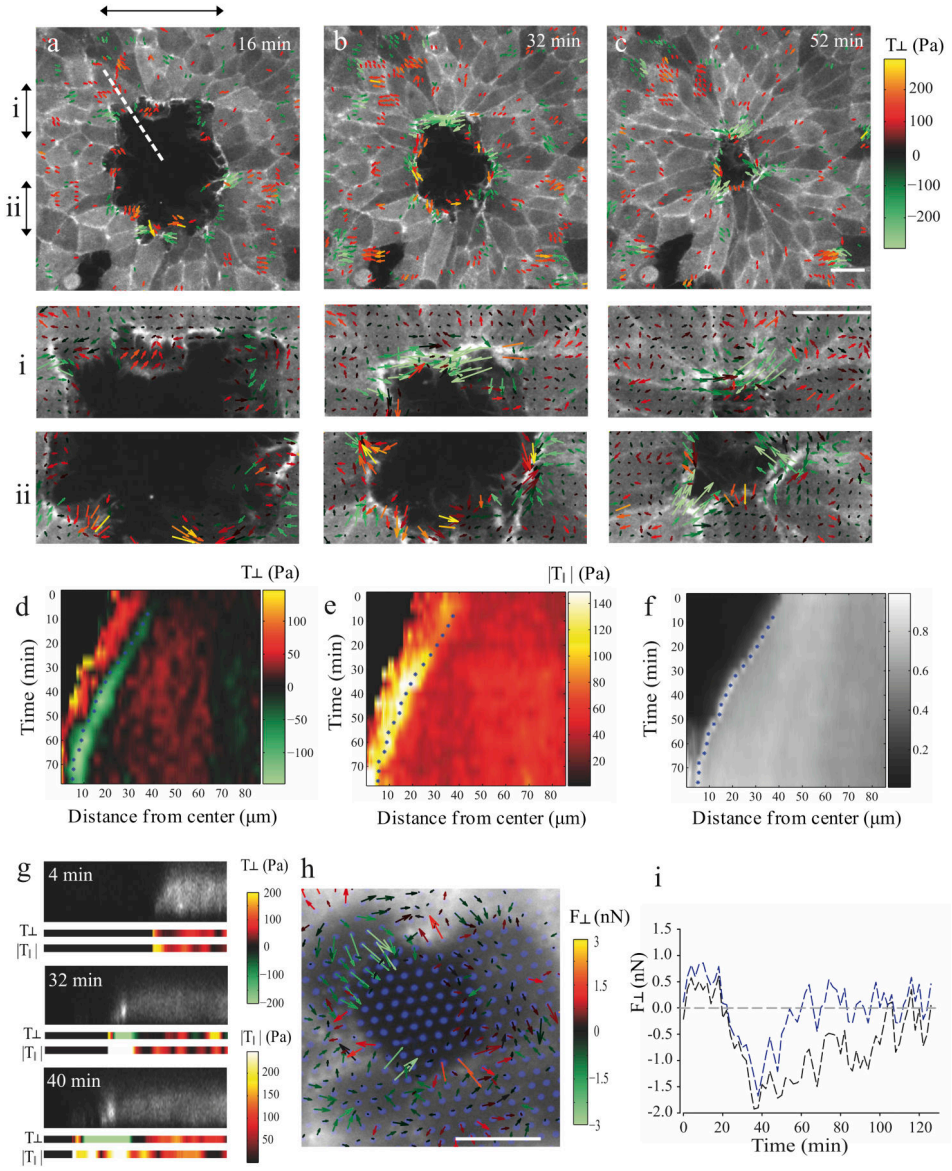

Figure 2. Traction forces during wound healing

(a-c) Vectorial representation of traction forces in LifeAct-GFP MDCK cells. Color coding is based on the values of the radial component, with positive forces pointing away from the wound. For clarity, values between −100 and 100 Pa were not plotted. Panels labeled as i and ii show a close-up of the regions indicated by arrows in panels a-c. Scale bar is 20 μm. (d) Kymograph for radial traction component $T_{\perp}$. (e) Kymograph for tangential traction component $T_{\parallel}$. (f) Kymograph of actin density based LifeAct-GFP fluorescence. Asterisks in panels d,e, and f show the position of the maximum actin density for each time point. (g) A

confocal z-section of LifeAct-GFP along the dashed line shown in Fig. 2a. Radial and tangential traction forces along that dashed line are shown below LifeAct-GFP images. Total length is 68 μm. (h) Traction force maps obtained using micropillar arrays (blue). Scale bar is 10 μm. Forces are color-coded according to the radial component. (i) Time-evolution of the radial forces of two distinct pillars. Positive forces point towards the wound exterior, whereas negative forces point towards the wound interior.

Europe PMC Funders Author Manuscripts

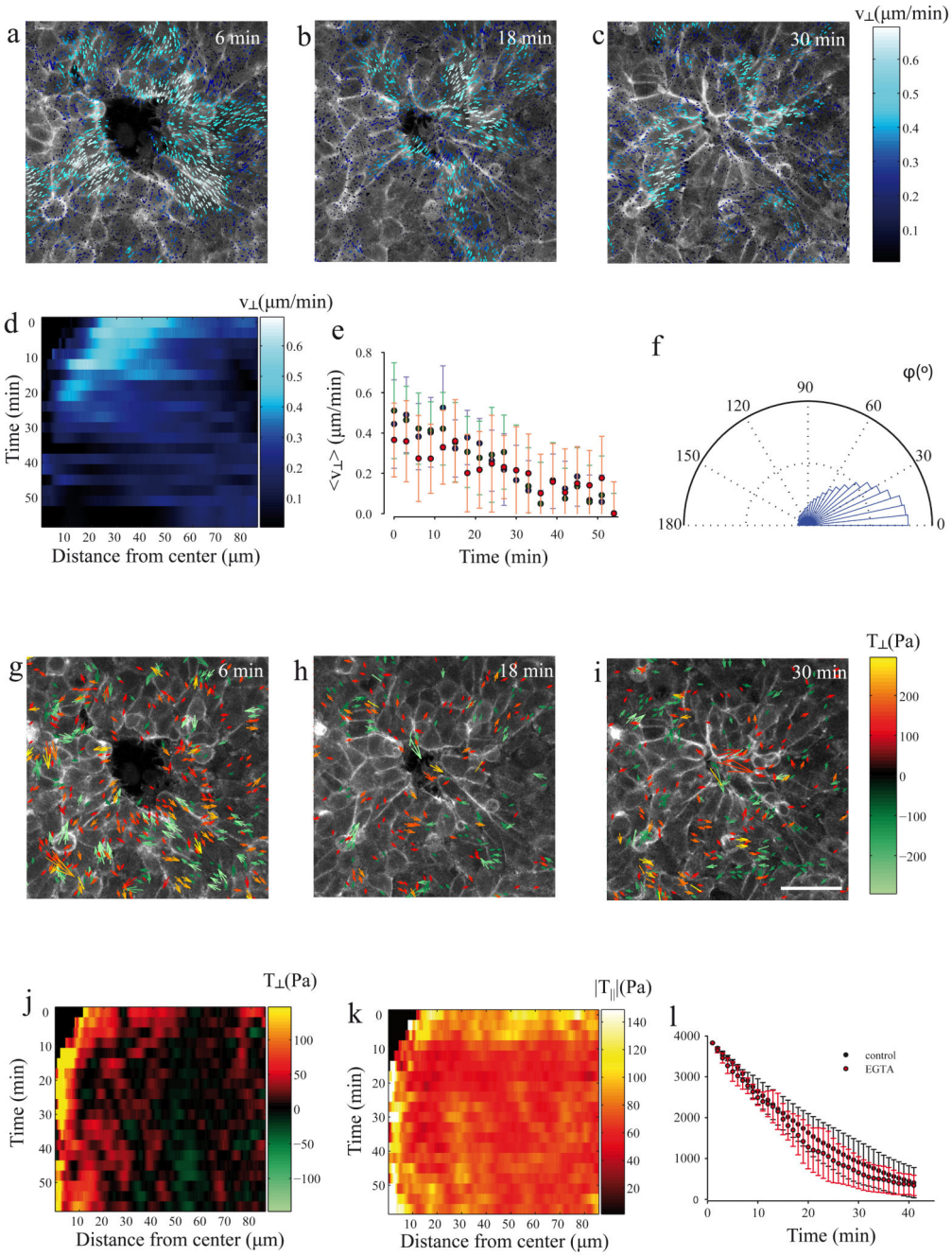

Figure 3. Traction forces in the absence of an actomyosin ring

(a-c) Vectorial plot of velocities measured by PIV. (d) Kymograph of the radial component of velocities. (e) Time evolution of velocities averaged over adjacent rings of width 15 μm (blue for cells located between 0-15 μm from the leading edge, green for 15-30 μm, red for 30-45 μm). Error bars represent standard deviation. (f) Angular distribution of the angle φ between cell velocities and the direction normal to the wound edge. (g-i) Vectorial representation of measured tractions. Color coding is based on the values of the radial component. For clarity, values between −100 and 100 Pa were not plotted. Kymographs of

Europe PMC Funders Author Manuscripts

radial (j) and tangential (k) components of traction forces. (l) Time evolution of the wound area in control cells and EGTA-treated cells. Error bars indicate standard deviation of n=5 (control) and n=6 (EGTA) samples. All scale bars are 40 μm.

Europe PMC Funders Author Manuscripts

Europe PMC Funders Author Manuscripts

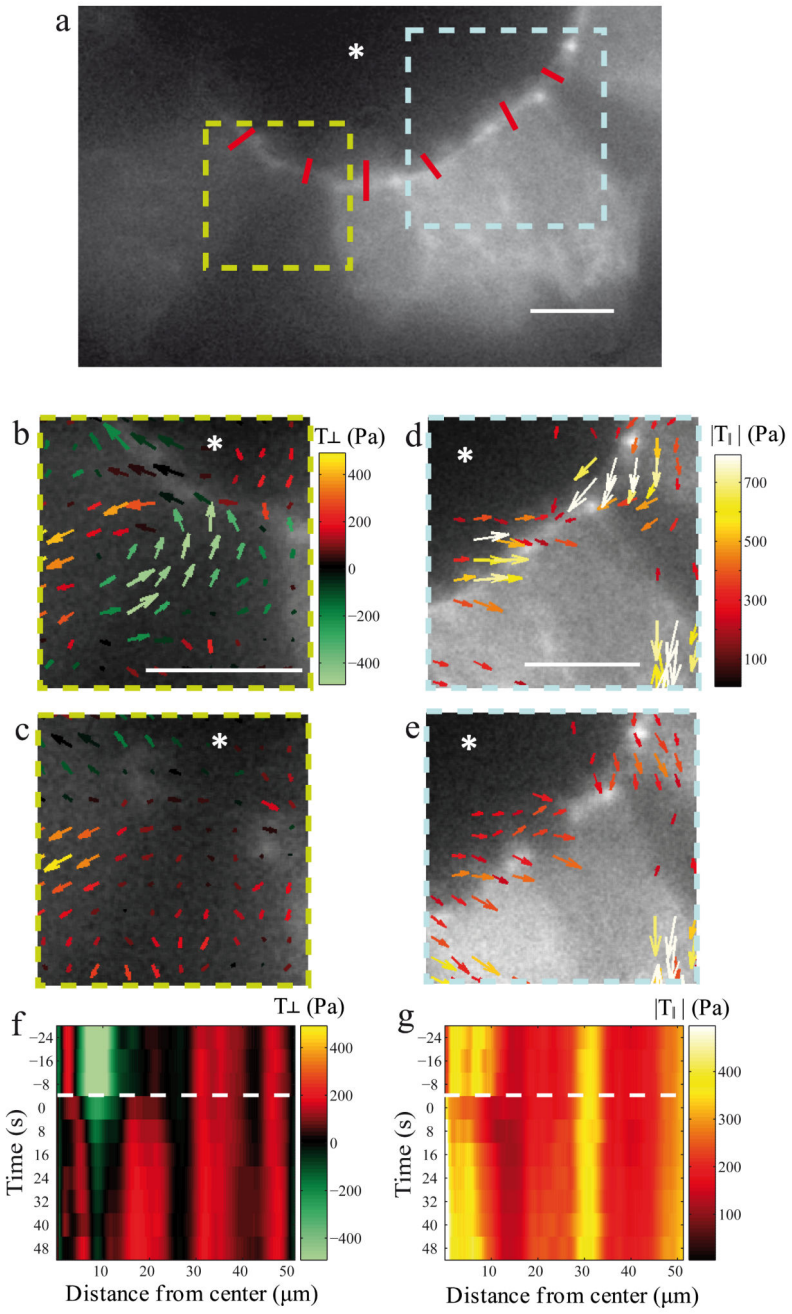

Figure 4. Traction forces after laser ablation of the actomyosin ring

(a) Fluorescence image of LifeAct-GFP cells prior to laser ablation. Red segments mark the sites of ablation. (b-c) A region displaying inward-pointing tractions before (b) and after (c) ring ablation. (c) Immediately after ablation, normal tractions were abrogated. (d-e) A region with strong tangential tractions before (d) and after ablation (e). (e) Tangential tractions were strongly attenuated by ring ablation. For clarity, only forces forming angles of less than 45° with the tangent were plotted. (f-g) Kymograph showing the time evolution of radial (f) and tangential (g) forces before and after ablation. The cut was performed immediately before

t=0s (dashed white line). All scale bars are 10 μm. Asterisks indicate the interior of the wound.

Europe PMC Funders Author Manuscripts

Europe PMC Funders Author Manuscripts

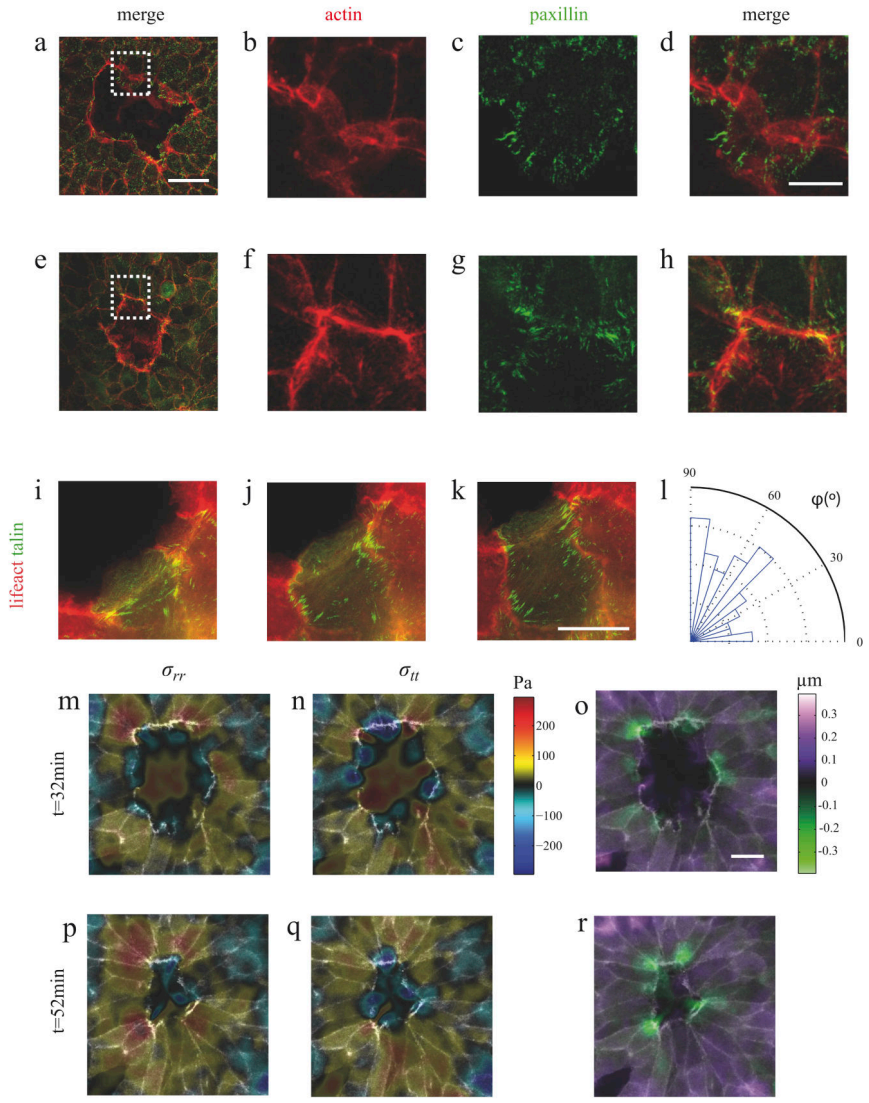

Figure 5. Force transmission from the ring to the substrate creates heterogeneous stresses and inward-pointing displacements of the underlying substrate

Representative immunofluorescence micrographs of paxillin and F-actin showing the characteristic structural organization of the leading edge during early (a-d) and late (e-h) stages of wound closure. (a-d) During initial stages, focal adhesions were localized at the tip of lamellipodia and were perpendicular to the leading edge. (e-h) During later stages, focal adhesions appeared under the actomyosin ring. (i-k) Time-lapse snap-shots of MDCK cells expressing LifeAct-Ruby and talin-GFP at three different time points of wound closure (see also Supplementary video 4). (l) Angular distribution of focal adhesion orientation with

respect to the normal direction (0° is normal to the ring, n=112 focal adhesions from 5 experiments). The analysis is performed in a 3 μm thick band located immediately behind the ring (including the ring). (m,p) Radial normal stress and (n,q) tangential normal stress in the upper surface of gel during the latest stages of wound closure. (o,r) Radial displacement of the gel surface. Negative displacements point towards the wound. The two time points considered in panels m to r correspond to panels b and c in Fig. 2. Scale bars are 40 μm for (a) and (e), 10 μm for (b-d) and (f-k), and 20 μm for (o).

Europe PMC Funders Author Manuscripts